Taper $PbZr_{0.2}Ti_{0.8}O_3$ Nanowire Arrays: From Controlled Growth by Pulsed Laser Deposition to Piezopotential Measurements

Yu-Ze Chen,[†,¶] Te-Hsiang Liu,[‡,¶] Cheng-Ying Chen,[§,⊥] Chin-Hung Liu,[†] Szu-Ying Chen,[†] Wen-Wei Wu,[‡] Zhong Lin Wang,[§] Jr-Hau He,[⊥] Ying-Hao Chu,[‡] and Yu-Lun Chueh[†,*]

[†]Department of Materials Science and Engineering, National Tsing Hua University, Hsinchu, 30013, Taiwan, R.O.C., [‡]Department of Materials Science and Engineering, National Chiao Tung University, Hsinchu, 30013, Taiwan, R.O.C., [§]School of Materials Science and Engineering, Georgia Institute of Technology, Atlanta, Georgia 30332-0245, United States, and [⊥]Department of Electrical Engineering and Institute of Photonics and Optoelectronics, National Taiwan University, Taipei 10617, Taiwan, R.O.C. [¶]These authors contributed equally to this work.

ABSTRACT Single crystalline $PbZr_{0.2}Ti_{0.8}$ (PZT) nanowires arrays (NWAs) with taper morphology were epitaxially grown on $SrTiO_3$ (STO) substrate using pulse laser deposition. The taper morphology was attributed to the overcoating of PZT layer *via* a lateral growth of PZT clusters/adatoms during PZT NW growth. The growth window for PZT film or nanowire was systematically studied at varied temperatures and pressures. The proposed growth mechanism of the taper PZT NWAs was investigated from a layer by layer growth *via* Frank–Van Der Merwe growth, followed by a formation of three-dimensional islands *via* Stranski–Krastanow growth, and then axial growth on the lowest energy (001) plane with growth direction of [001] *via* vapor–solid growth mechanism. However, under certain conditions such as at higher or lower pressure (>400 or <200 mTorr) or substrate temperatures (>850 °C and <725 °C), formation of the PZT NWs is suppressed while the epitaxial PZT thin film *via* the layer-by-layer growth remains. The controllable growth directions of the PZT NWAs on (001), (110), and (111) STO substrates were demonstrated. The piezopotential of the taper PZT NWAs using a conducting atomic force microscope with the average voltage output of ~18 mV was measured. The theoretical piezopotential of a PZT NW was calculated to compare with the measured outputs, providing a comprehensively experimental and theoretical understanding of the piezoelectricity for the PZT NW.

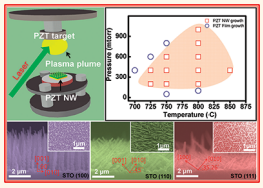

KEYWORDS: pulsed laser deposition · PZT nanowire arrays · piezopotential · vapor-solid growth

Complex oxide materials typically have a variety of outstanding features, such as ferroelectricity,[1] piezoelectricity,[2] and superconducting,[3] which are broadly applied to the energy field and the electronic devices, such as nonvolatile memories,[4] micromotors,[5] and sensors,.[6] Among complex metal oxides, lead–zirconium–titanium (PZT) with a provskite structure in the ferroelectric group is the most promising complex oxide material with extraordinary high dielectric constant, large hysteresis, and excellent piezoelectric coefficient, which can be readily incorporated with current piezoelectric and energy-harvesting devices.

Up to now, a variety of synthetic approaches for PZT nanowires (NWs) had been proposed, such as hydrothermal,[7,8] template infiltration,[9] and electrophoresis.[10] Nevertheless, there are many restrictions on these approaches, for example, the requirement of metal catalysts for the growth of PZT during the hydrothermal process. In the case of template infiltration and electrophoresis processes, the critical dimension requirements on the nanosize templates have set limitations on fabrications of nanostructured PZTs. In this regard, we demonstrated the growth of single-crystalline PZT NW arrays (NWAs) with taper morphology by the pulsed laser deposition technique, which provides the advantage of controlling stoichiometry at a lower temperature process compared with other deposition techniques.[11] The detailed growth window for whether PZT thin films or PZT NWs were formed was successfully explored. The microstructure of the taper PZT NWs at each growth stage was investigated to determine the growth mechanism. Controllable orientations of the PZT NWAs along the [001], [110], and [111] directions were demonstrated, depending on underlying substrate orientations. The piezopotential of the taper PZT NWAs was measured using atomic force microscopy (AFM), and the theoretical piezopotential of a PZT NW was calculated to compare with the measured outputs, shedding light on the intrinsic properties of nanoscale PZT nanowires.

* Address correspondence to ylchueh@mx.nthu.edu.tw.

Received for review January 25, 2012 and accepted February 29, 2012.

Published online February 29, 2012
10.1021/nn300370m

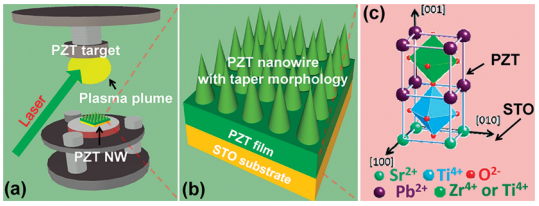

Figure 1. (a) Fabrication process of PZT NWAs *via* PLD technique; (b) schematic growth of taper PZT NWAs on a STO substrate; (c) a hard ball model of PZT unit cell stacking on STO lattice.

RESULTS AND DISCUSSION

Figure 1a schematically illustrates how we performed the pulsed laser deposition (PLD) to synthesize PZT NWAs. A KrF excimer laser with a wavelength of 248 nm and adjustable frequencies from 1 to 20 Hz was used to ablate a quaternary $PbZr_{(1-x)}Ti_xO_3$ target where x ranges from 0.2 to 0.8. PZT NWAs were found to grow on $SrTiO_3$ (STO) substrates with substrate temperatures maintained at 700−850 °C during deposition. The corresponding schematic of taper PZT NWAs on a STO substrate is shown in Figure 1b. During the growth process, a PZT thin film was found to epitaxially form on the STO substrate first, followed by the growth of the PZT NWAs. An atomic structure model between the PZT NWAs and the STO substrate is drawn in Figure 1c.

To explore the growth window of the PZT NWAs on the STO substrate, a series of systematic experiments were conducted, including different substrate temperatures and pressures with the laser frequency and the distance between PZT target and substrate holder fixed at 10 Hz and 4 cm, respectively. Figure 2a−g shows scanning electron microscopy (SEM) images of the PZT NWAs grown at different substrate temperatures ranging from 700 to 850 °C with a growth pressure of 400 mTorr. The taper morphology with the base and the tip widths of *ca.* 100−150 nm and *ca.* 30−60 nm, respectively, can be clearly observed. Note that the as-grown PZT epitaxial film was formed initially and then the PZT NWAs were nucleated and grown from the epitaxial PZT film at specific conditions. It was found that the PZT NWAs could be formed at substrate temperatures ranging from 750 to 850 °C while the formation of the PZT film on the STO substrate is preferred as substrate temperatures <700 °C and/or >850 °C (Supporting Information, Figure S1). Figure 2h shows lengths of the PZT NWAs and thicknesses of the underlying PZT film as a function of substrate temperatures. As substrate temperature increased, the length of PZT NWAs increased while the thickness of the underlying PZT film decreased. The maximum length of PZT NWAs is 1.3 μm with a minimum thickness of *ca.* 90−100 nm for the underlying PZT thin film at the substrate temperatures of *ca.* 800−825 °C. PZT thin films are preferred for lower (<100 mTorr) and higher (>800 mTorr) working pressures, whereas the growth of PZT NWAs can only exist at pressures from ~200 to 700 mTorr at a substrate temperature of 750 °C for 20 min (see Supporting Information, Figures S2a−d). Furthermore, other growth parameters, such as a distance between PZT target and substrate at 4 cm and a laser frequency of 10 Hz were also optimized as shown in Supporting Information, Figures S2 and S4. Therefore, a plot for the selective growth of PZT NWs or PZT film based on the pressures and the substrate temperatures can be constructed as shown in Figure 2i.

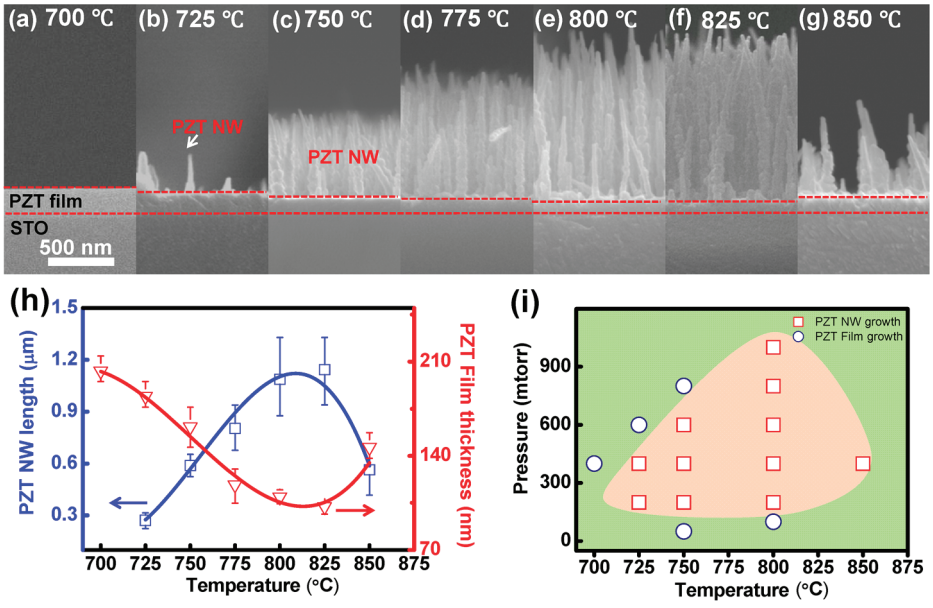

Figure 2. SEM images of vertically aligned taper PZT nanowires with a fixed pressure of 400 mTorr and growth time of 20 min at varied growth temperatures of (a) 700, (b) 725, (c) 750, (d) 775, (e) 800, (f) 825, and (g) 850 °C; (h) the lengths of taper PZT NW and the thicknesses of underlying PZT film as the function of growth temperatures; (i) a plotted window for the growth of the PZT NW or film extracted from different growth pressures and substrate temperatures.

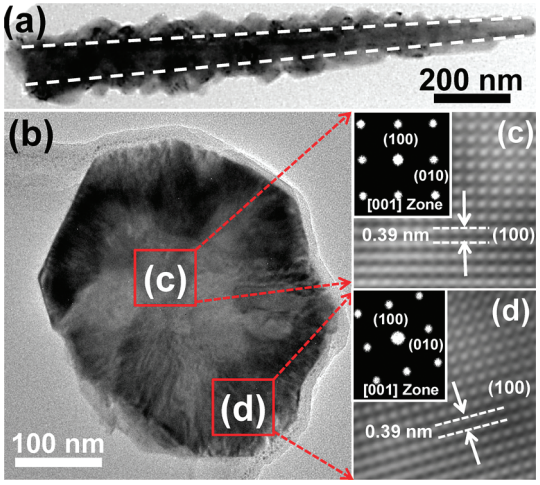

Figure 3. (a) A TEM image of a PZT nanowire with taper morphology; (b) a cross-sectional TEM image of the PZT nanowire observed along [001] direction; (c) the corresponding HRTEM image taken from the core region of the PZT nanowire, with which the lattice spacing of 0.39 nm for (100) plane is indexed. Inset shows the diffraction pattern with [001] zone axis extracted by fast Fourier transform, indicating the growth direction of PZT nanowire being along [001]. (d) The HRTEM image taken from shell region. Inset shows the corresponding diffraction pattern with [001] zone axis.

Figure 3a shows a low magnified transmission electron microscopy (TEM) image of a PZT nanowire with taper morphology. It is obvious that the taper PZT nanowire consists of two parts, namely, an inner nanowire body core and an outer uniform PZT overcoating layer. The outer uniform overcoating layer is believed to be the main reason for the taper morphology. To shed light on the difference between two regions, focused ion beam (FIB) was used to cut the PZT nanowire, which is perpendicular to the nanowire axis for the cross-sectional TEM observation as shown in Figure 3b. The corresponding high resolution TEM (HRTEM) results are shown in Figure 3c,d taken from rectangular areas marked as c and d in Figure 3b, where a different contrast at two regions was observed. Insets in Figure 3c,d reveal the selective diffraction patterns with [001] zone axis converted by fast Fourier transform (FFT). The HRTEM images from two regions indicate the single crystal feature, for which planar spacings of 0.39 nm for region c and 0.39 nm for region d were found that completely match with the (100) plane for two regions, respectively. In addition, atomic concentrations are ~21 atom % Pb, ~5 atom % Zr, ~15 atom % Ti, ~59 atom % O for region c and ~20 atom % Pb, ~6 atom % Zr, ~17 atom % Ti, ~57 atom % O for region d, which perfectly agree with the concentration of the PZT target, namely, $PbZr_{0.2}Ti_{0.8}O_3$. Therefore, a possible reason for different contrast found in the two regions is most likely attributed to the different scattering behavior of electrons because of the different crystal stacking orientation confirmed by different patterns (insets in Figure 3c,d).

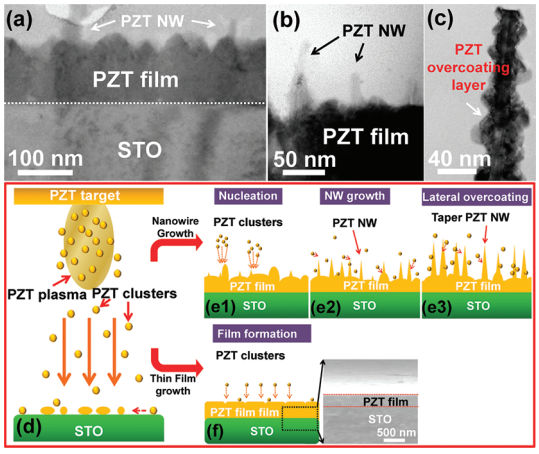

Figure 4. (a) A cross-sectional image of the PZT NWs grown on a STO substrate at very initial condition with a growth time of 30 s, growth pressures of 400 mTorr, and substrate temperature of 750 °C. (b) A cross-sectional image of the PZT NWs grown on the STO substrate at the identical growth conditions with the growth time extending to 2 min. (c) The magnified TEM image of the PZT overcoating layer. (d–f) Schematics of growth mechanism for PZT NWAs with taper morphology and PZT film.

To investigate the growth mechanism of the PZT nanowire, we separate the growth of PZT NW into three stages according to growth time. Figure 4a shows that the first stage that the PZT thin film was grown first, followed by the second stage, the growth of the taper PZT NWs at the substrate temperature of 750 °C and the pressure of 400 mTorr for growth time of 30 s. The longer the growth time, the longer the PZT NW is as shown in Figure 4b. Figure 4c illustrates the third stage with the formation of an overcoating layer. Accordingly, two possible mechanisms could be inferred for our case, namely, vapor–solid growth mechanism (VS)[12] and catalytic vapor–liquid–solid (VLS) mechanism.[13] According to the round shape at the tip region of nanowire observed from SEM images and no catalytic metals confirmed from the TEM image as shown in Figure 4 images a and b, the catalytic VLS mechanism in our case could be ruled out. Therefore, the possible growth mechanism of the taper PZT NWs was resulted from the VS growth mechanism, which is mostly occurred at metal oxide materials because of an anisotropic crystalline feature. A well-known two-dimensional (2D) nucleation probability, which highly relies on a surface free energy difference at the different planes is typically used to explain the growth model.[14] An atom absorbed on the lower surface plane has higher binding energy (lower interaction energy), resulting in a higher 2D nucleation probability. Consequently, the growth of the 1D nanowire along the axial direction could be achieved. In addition, the structure defects, such as stacking faults and microtwins may also play an important role as the nucleation seeds/sites.[15] The proposed mechanism for the formation of the taper PZT nanowire on the STO substrate is

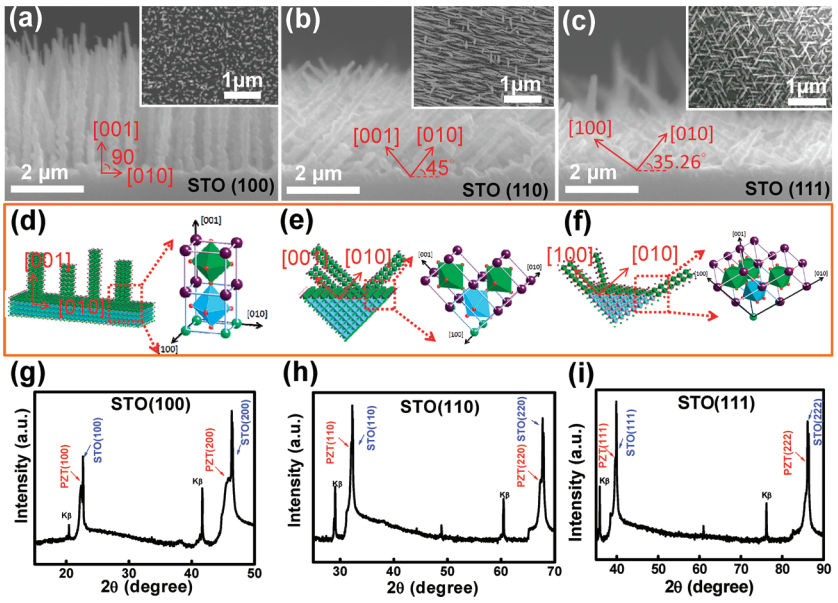

Figure 5. SEM images of PZT NWAs grown on STO substrates with (a) (100), (b) (110), and (c) (111) orientations. Hard ball models for the growth of PZT NWAs on STO substrates with (d) (100), (e) (110), and (f) (111). (g–i) The corresponding XRD results of the PZT NWAs grown on STO substrates with different orientations.

schematically illustrated in Figure 4d–f. In an early stage, PZT molecules from the PZT target prefer to epitaxially assemble on the STO substrate *via* Frank–Van Der Merwe (FV) growth, namely, a layer by layer growth, for which the specific surface free energy of STO–vacuum (γ_s) is larger than that of STO–PZT film (γ_i)+PZT film–vacuum (γ) as show in Figure 4d.[16] However, elastic relaxation energy resulting from lattice mismatch between the PZT film and the STO substrate increases with an increase of the PZT film thickness. At the PZT film thickness over a critical value, the formation of coherent 3D islands is preferred rather than the smooth film growth, allowing a significant reduction of total energy due to the later elastic relaxation of 3D islands against coarsening (Ostwald ripening) *via* Volmer–Weber growth (VW),[17] which is typically called the Stranski–Krastanow (SK) growth model[18] (Figure 4e1). The newly arriving PZT clusters/atoms are preferably and epitaxilly formed on these as-grown PZT 3D islands owing to the reduction of surface free energy, resulting in the formation of PZT NW along [001] direction *via* VS growth, which restricts the lateral growth as shown in Figure 4e2 since (001) is the lowest surface energy surface. The results are also consistent with the NW growth direction of [001] observed by the TEM image (Figure 3). Once the PZT NWs start to grow, the lateral diffusion of PZT clusters/adatoms, namely, lateral overcoating along the side well of the PZT NWs could occur as well, thereby forming the taper morphology as shown in Figure 4e3. In contrast, under certain condition such as higher pressures or certain substrate temperatures (>850 °C and <725 °C), the formation of PZT NWs was suppressed, and then epitaxial growth of PZT thin film could continue in a layer-by-layer formation, which corresponds to the FV-type as shown in Figure 4f. In addition, we also tried to control different Zr/Ti ratios from 20/80 atom % to 80/20 atom % of the PZT NWAs by controlling the PZT targets with different Zt/Ti ratios while the PZT NWAs can only be achieved at the Zr/Ti ratio of 20/80 at % as shown in Figure S5 (Supporting Informatioin).

An unique feature of our PZT NWAs growth is to precisely control orientations of the taper PZT NWAs. To demonstrate this concept, STO substrates with different substrate orientations including (001), (110), and (111) were prepared. SEM images after growth were shown in Figure 5a–c and insets show the corresponding top-view SEM images. Angles between the PZT NWAs and the underlying STO substrate are found at ~90°, ~45°, and ~35.26° on (001), (110), and (111) STO substrates as schematically drawn in Figure 5 panels a and b, and c, respectively. The results confirm the ability to precisely control the NW growth directions at different substrate orientations and also explain that PZT clusters prefer to epitaxially grow on the {100} family plane because of the smallest surface free energy compared with that of other planes, which matches well with our proposed growth model. In addition, the growth of the PZT NWs from the STO substrate based on hard ball models was illustrated in Figure 5d–f to clearly reveal the precisely controlled ability of the PZT NWAs by different substrate orientations. Figure 5 panels g–i show the corresponding X-ray diffraction (XRD) spectra of the PZT NWAs at different STO substrates, confirming the epitaxial relationship between the PZT NWAs and the STO substrates.

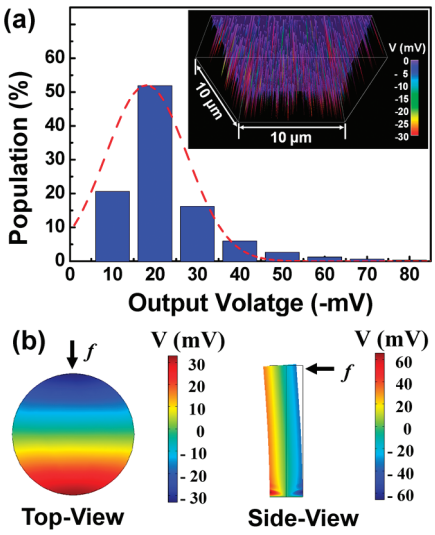

Figure 6. (a) A statistical distribution of the measured piezopotential output where an average piezopotential output is *ca.* −18 mV. Inset shows a three-dimensional (3D) plot of piezopotential output with a scanning area of 10 × 10 μm^2 where the different colors represent the magnitude of the output potential. (b) The calculated top-view and side-view piezopotential distributions in a PZT NW bent by an AFM cantilever.

The PZT is a typical piezoelectric material with a larger piezoelectric constant.[19,26,27] Its piezoelectric domain can be aligned by applying an electric poling along the length direction of the nanowires. To investigate the piezoelectric properties of the PZT NWAs, an atomic force microscope in contact mode using a Pt-coated Si tip as a cantilever was used to scan across the vertically aligned PZT NWAs with the appropriate lengths of *ca.* 100−200 nm, where the cantilever has a spring constant of 1.55 N/m with a constant normal force of 5 nN maintained between the tip and the PZT NWAs surface.[22−24] Through scanning the tip across the NWAs, the piezoelectric output voltages were monitored by an external load (500 MΩ) without an external voltage applied during the measurements. For a sample that was grown under different condition and has relatively uniform shape, the statistical distribution of the measured piezoelectric output is plotted in Figure 6a, and the inset in Figure 6a shows a three-dimensional (3D) plot of the piezopotential output from the PZT NWAs with a scanning area of 10 × 10 μm^2, where the different colors represent the magnitude of the output potential. Obviously, the piezoelectric outputs show a statistical distribution of *ca.* 80−85% output voltages within −10 to −30 mV with average piezoelectric output of *ca.* −18 mV, which is comparable to that of the ZnO NWAs.[22−24] To predict the measured piezoelectric output, Lippman theory was utilized to calculate the piezopotential distribution in a bent PZT NW under a lateral force (*f*) of 80 nN with the [001]-orientated PZT NW of ∼200 nm in length and 50 nm in diameter.[24,25] (see the Supporting Information for more detailed information) A semiquantitative comprehension can be realized by a numerical calculation without considering the carrier concentration by taking the following values into account: relative dielectric constants of PZT ($\kappa_\perp$ = 504.1, $\kappa_\parallel$ = 270), the density (ρ = 7600 *kg*/m^3), the anisotropic elastic constants (C_{11} = 134.8680 GPa, C_{12} = 67.8883 GPa, C_{13} = 68.0876 GPa, C_{33} = 113.297 GPa, C_{44} = 22.2222 GPa), and the piezoelectric constants (e_{15} = 9.77778 C/m^2, e_{31} = −1.81603 C/m^2, e_{33} = 9.05058 C/m^2).[24,25]

The calculated top-view and side-view of piezopotential distributions in the PZT NW bent by an AFM tip is shown in Figure 6b. Clearly, the maximum negative piezopotential of *ca.* −30 mV as shown in the left-hand side of Figure 6b drives the free electrons across the external load (500 MΩ) as the AFM tip scans across the NW, forming a transient current. However, the measured piezopotential is expected to significantly depend on contact resistance between the Pt tip and the NWs, contact resistance between Ag pastes and PZT films at the bottom of the NWs, resistance of the bottom PZT film, and limited conductivity with small capacitance of the NWs, resulting in lower measured piezopotentials (−18 mV) than the calculated one (−30 mV). Interestingly, no external electric poling was applied to create the piezoelectricity at our PZT NWAs while the piezopotentials could be still measured. We believed that the origin of piezoelectricity in our PZT NWAs is most likely from the self-polarization effect resulting from (1) accumulation of oxygen vacancies at the interface between epitaxial PZT films/STO substrates and PZT NW/PZT film, (2) trapping of free electrons at the interfaces, and (3) the oxygen vacancy defective dipole complexes throughout the PZT film during nanowire growth, which has been observed in other reports.[26,27] The self-polarization phenomenon is still unclear yet and further investigation is needed.

CONCLUSIONS

Growth of single-crystalline taper PZT NWAs by PLD was demonstrated successfully. The detailed growth window of a PZT thin film or PZT nanowire was constructed at varied pressures and temperatures. The taper morphology of PZT NWAs was attributed to an overcoating of the PZT layer from a lateral growth of PZT clusters during NW growth. The growth mechanism of the taper PZT NWAs was found to be layer-by-layer growth (FV model) to a formation of 3D islands (SK model), followed by an axial growth along the lowest (001) plane *via* the VS growth mechanism. However, under certain growth conditions such as higher or lower pressure (>400 mTorr or <200 mTorr) and higher or lower substrate temperatures (>850 °C and <725 °C), the formation of PZT NWs is suppressed, and the epitaxial PZT film remains and grows *via* the layer-by-layer growth. A unique advantage of our PZT

NWAs growth is the precise control of the taper PZT NWAs with different orientations where the angles between the PZT NWAs and the underlying STO substrate at ~90°, ~45°, and ~35.26° on (001), (110), and (111) STO substrates were demonstrated, respectively. The electricity generation from individual vertically aligned PZT NWAs with the average voltage output of ~18 mV was measured by AFM. The measured outputs were analyzed in reference to the theoretically calculated piezopotential distribution in a bent NW, providing a comprehensive experimental and theoretical base for understanding the piezoelectricity of a single PZT NW, which will be an alternate material for the design and optimization of high performance nanogenerators.

METHODS

Fabrication of PZT NWs Arrays and PZT Thin Film. PZT NWAs were epitaxially grown on precleaned 1 × 1 cm^2 $SrTiO_3$ (STO) substrates by a pulse laser deposition (PLD) system equipped with a heating substrate holder and a KrF excimer laser with a wavelength at 248 nm and power of 250 mJ. Epitaxial PZT NWs with pervoskite phase were formed by evaporating a single quaternary $PbZr_{(1-x)}Ti_xO_3$ target with different atomic ratios of Pb:Zr:Ti:O. Dynamic chamber pressures from 100 to 1000 mTorr were controlled by O_2 gases and the substrate holder temperatures of 700−850 °C were maintained during the deposition. The working distance between the PZT target and the substrate holder was set at 2.5−6 cm with the laser frequencies of 1−20 Hz.

Characterizations. The morphology of PZT NWAs was studied by field-emission scanning electron microscopy (FE-SEM, JSM-6500F, JEOL), and their crystalline structures were characterized by X-ray diffraction (XRD, D2 Phaser, Bruker) with Cu Kα radiation (λ = 0.154 nm). A field-emission transmission electron microscope (JEM-3000F, operated at 300 kV with point-to-point resolution of 0.17 nm) equipped with an energy dispersion spectrometer (EDS) was used to obtain the information of the microstructures and the chemical compositions. Piezoelectric measurements were performed using AFM (molecular force probe MFP-3D from Asylum Research) with a conducting Pt-coated Si tip (14 μm in height with an apex angle of 70°, from Olympus). The output voltage across an outside load of resistance R_L (500 MΩ) was continuously monitored as the tip scanned over the NWs. No external voltage was applied during the experiment measurements.

Conflict of Interest: The authors declare no competing financial interest.

Acknowledgment. This research was supported by the National Science Council through Grant Nos. NSC 100-2628-E-007-003, NSC 98-2112-M-007-025-MY3, NSC 100-2119-M-009-003, and Low Carbon Energy Research Center, National Tsing Hua University through Grant No, 100N2024E1. C.Y.C. would like to thank the Graduate Students Study Abroad Program sponsored by National Science Council (NSC100-2917-I-002-009).

Supporting Information Available: SEM images of PZT NWAs grown at 700 °C for different growth time from 10 to 40 min; SEM images of PZT NWAs grown at different pressures from 100 to 800 mTorr; SEM images of PZT NWAs grown at different distances from 2.5 to 6 cm between PZT target and STO substrate; SEM images of PZT NWAs grown at different laser frequencies from 1 to 20 Hz; SEM images of PZT NWAs using different PZT targets with different Zr/Ti ratios; Piezopotential simulation. These materials are available free of charge *via* the Internet at http://pubs.acs.org.

REFERENCES AND NOTES

1. Wang, J.; Neaton, J. B.; Zheng, H.; Nagarajan, V.; Ogale, S. B.; Liu, B.; Viehland, D.; Vaithyanathan, V.; Schlom, D. G.; Waghmare, U. V.; *et al*. Epitaxial $BiFeO_3$ Multiferroic Thin Film Heterostructures. *Science* **2003**, *299*, 1719–1722.
2. Eerenstein, W.; Mathur, N. D.; Scott, J. F. Multiferroic and Magnetoelectric Materials. *Nature* **2006**, *442*, 759–765.
3. McCammon, C. Perovskite as a Possible Sink for Ferric Iron in the Lower Mantle. *Nature* **1997**, *387*, 694–696.
4. Araujo, C. A.-P. d.; Cuchiaro, J. D.; McMillan, L. D.; Scott, M. C.; Scott, J. F. Fatigue-Free Ferroelectric Capacitors with Platinum Electrodes. *Nature* **1995**, *374*, 627–629.
5. Tuchiya, T.; Itoh, T.; Sasaki, G.; Suga, T. Preparation and Properties of Piezoelectric Lead Zirconate Titanate Thin Films for Microsensors and Microactuators by Sol-Gel Processing. *J. Ceram. Soc. Jpn.* **1996**, *104*, 159–163.
6. Zhang, Q.; Whatmore, R. W. Sol-Gel PZT and Mn-Doped PZT Thin Films for Pyroelectric Applications. *J. Phys. D: Appl. Phys.* **2001**, *34*, 2296–2301.
7. Xu, G.; Ren, Z.; Du, P.; Weng, W.; Shen, G.; Han, G. Polymer-Assisted Hydrothermal Synthesis of Single-Crystalline Tetragonal Perovskite $PbZr_{0.52}Ti_{0.48}O_3$ Nanowires. *Adv. Mater.* **2005**, *17*, 907–910.
8. Wang, J.; Sandu, C. S.; Colla, E.; Wang, Y.; Ma, W.; Gysel, R.; Trodahl, H. J.; Setter, N.; Kuball, M. Ferroelectric Domains and Piezoelectricity in Monocrystalline $Pb(Zr,Ti)O_3$ Nanowires. *Appl. Phys. Lett.* **2007**, *90*, 133107–3.
9. Hernandez, B. A.; Chang, K.-S.; Fisher, E. R.; Dorhout, P. K. Sol−Gel Template Synthesis and Characterization of $BaTiO_3$ and $PbTiO_3$ Nanotubes. *Chem. Mater.* **2002**, *14*, 480–482.
10. Limmer, S. J.; Seraji, S.; Forbess, M. J.; Wu, Y.; Chou, T. P.; Nguyen, C.; Cao, G. Z. Electrophoretic Growth of Lead Zirconate Titanate Nanorods. *Adv. Mater.* **2001**, *13*, 1269–1272.
11. Smith, H. M.; Tuner, A. F. Vacuum Deposited Thin Films Using a Ruby Laser. *Appl. Opt.* **1965**, *4*, 147–148.
12. Yang, P.; Lieber, C. M. Nanostructured High-Temperature Superconductors: Creation of Strong-Pinning Columnar Defects in Nanorod/Superconductor Composites. *J. Mater. Res.* **1997**, *12*, 2981–2996.
13. Stach, E. A.; Pauzauskie, P. J.; Kuykendall, T.; Goldberger, J.; He, R.; Yang, P. Watching GaN Nanowires Grow. *Nano Lett.* **2003**, *3*, 867–869.
14. Yin, Y.; Zhang, G.; Xia, Y. Synthesis and Characterization of MgO Nanowires Through a Vapor-Phase Precursor Method. *Adv. Funct. Mater.* **2002**, *12*, 293–298.
15. Zhao, L. X.; Meng, G. W.; Peng, X. S.; Zhang, X. Y.; Zhang, L. D. Large-Scale Synthesis of GaN Nanorods and Their Photoluminescence. *Appl. Phys. A* **2002**, *74*, 587–590.
16. Springholz, G.; Frank, N.; Bauer, G. The Origin of Surface Roughening in Lattice-Mismatched Frank van der Merwe Type Heteroepitaxy. *Thin Solid Films* **1995**, *267*, 15–23.
17. Volmer, M.; Weber, A. Nucleus Formation in Supersaturated Systems. *Z. Phys. Chem* **1926**, *119*, 277.
18. Stranski, I. N.; Krastanov Theory of Orientation Separation of Ionic Crystals. *Acad. Wiss. Math.- Naturwiss. Klasse IIb* **1938**, 797.
19. Shaoping, L.; Cao, W.; Cross, L. E. Stress and Electric Displacement Distribution Near Griffith's Type III Crack Tips in Piezoceramics. *Mater. Lett.* **1990**, *10*, 219–222.
20. Xu, S.; Hansen, B. J.; Wang, Z. L. Piezoelectric-Nanowire-Enabled Power Source for Driving Wireless Microelectronics. *Nat. Comm.* **2010**, *1*, 93.
21. Chen, X.; Xu, S.; Yao, N.; Shi, Y. 1.6 V Nanogenerator for Mechanical Energy Harvesting Using PZT Nanofibers. *Nano Lett.* **2010**, *10*, 2133–2137.
22. Wang, Z. L.; Song, J. Piezoelectric Nanogenerators Based on Zinc Oxide Nanowire Arrays. *Science* **2006**, *312*, 242–246.
23. Wang, Z. L.; Rusen, Y.; Zhou, J.; Qin, Y.; Xu, C.; Hu, Y.; Xu, S. Lateral Nanowire/Nanobel Based Nanogenerators, Piezotronics and Piezo-Phototronics. *Mater. Sci. and Engi. Reports.* **2010**, *R70*, 320–329.

24. Chen, C.-Y.; Huang, J.-H.; Song, J.; Zhou, Y.; Lin, L.; Huang, P.-C.; Zhang, Y.; Liu, C.-P.; He, J.-H.; Wang, Z. L. Anisotropic Outputs of a Nanogenerator from Oblique-Aligned ZnO Nanowire Arrays. *ACS Nano* **2011**, *5*, 6707–6713.
25. Gao, Y.; Wang, Z. L. Equilibrium Potential of Free Charge Carriers in a Bent Piezoelectric Semiconductive Nanowire. *Nano Lett.* **2009**, *9*, 1103–1110.
26. Pike, G. E.; Warren, W. L.; Dimos, D.; Tuttle, B. A.; Ramesh, R.; Lee, J.; Keramidas, V. G.; Evans, J. T. Voltage Offsets in (Pb, La)(Zr,Ti)O_3 Thin Films. *Appl. Phys. Lett.* **1995**, *66*, 484–487.
27. Afanasjev, V. P.; Petrov, A. A.; Pronin, I. P.; Tarakanov, E. A.; Kaptelov, E. J.; Graul, J. Polarization and Self-Polarization in Thin $PbZr_{1-x}Ti_xO_3$ (PZT) Films. *J. Phys.: Condens. Matter* **2001**, *13*, 8755–8763.